View metadata, citation and similar papers at core.ac.uk
brought to you by CORE
provided by University of Liverpool Repository

Numerical investigation of the spatiotemporal distribution of chemical species in atmospheric surface barrier-discharge

M I Hasan and J L Walsh

Department of Electrical Engineering and Electronics, the University of Liverpool,

Brownlow Hill, L69 3GJ, U.K.

E.mail: jlwalsh@liverpool.ac.uk

Abstract: Using a 1D time dependent convection-reaction-diffusion model, the temporal and spatial distributions of species propagating downstream of an atmospheric pressure air surface barrier discharge was studied. It was found that the distribution of negatively charged species is more spatially spread compared to positive ions species, which is attributed to the diffusion of electrons that cool down and attach to background gas molecules, creating different negative ions downstream of the discharge region. Given the widespread use of such discharges in applications involving the remote microbial decontamination of surfaces and liquids, the transport of plasma generated reactive species away from the discharge region was studied by implementing mechanical convection through the discharge region. It was shown that increased convection causes the spatial distribution of species density to become uniform. It was also found that many species have a lower density close to the surface of the discharge as convection prevents their accumulation. While for some species, such as NO_2, convection causes a general increase in the density due to a reduced residence time close to the discharge region, where it is rapidly lost through reactions with OH. The impact of the applied power was also investigated and it was found that the densities of most species, whether charged or neutral, are directly proportional to the applied power.

1. Introduction

Atmospheric-pressure air plasma systems have attracted considerable interest in recent years as low-cost and simple sources of chemically reactive species [1-3]. It has been shown experimentally that these types of discharges consume little electrical energy, are scalable to cover large areas and operate at ambient temperatures [4]. Significantly, such plasmas are capable of generating large fluxes of chemically active species that have powerful antimicrobial properties including O, O_3, NO_2, H_2O_2, and O_2^- [5], making them suitable for sterilization [6,7], wound treatment [8,9], dental hygiene [10,11], and other biomedical applications [12,13].

One of the most common atmospheric-pressure discharge configurations is the Surface Barrier Discharge SBD (also known as Surface Micro-Discharge SMD) [14,15]. In this configuration, a grid-like metallic electrode is adhered to a dielectric surface. On the opposite side of the dielectric material, a second conducting surface is attached to form a dielectric barrier discharge configuration. When a sufficiently high voltage is applied, plasma forms around the edges of the metallic electrode and spreads across the dielectric surface, making a relatively uniform discharge on the surface. This configuration is easily scalable by placing many discharges in an array, opening the gateway to applications such as food decontamination on an industrial scale.

The nature of the chemical species produced by an SBD are highly dependent on the electrode geometry and applied voltage waveform; as such, there is a real need to fully characterize and optimize a given discharge for a given application. There have been a limited number of studies, either experimental or theoretical, on the influence of discharge parameters and electrode geometry on species production and transport in an SBD discharge. Given the complexity of the discharge chemistry, numerical studies are faced with a large number of species and chemical reactions, imposing a considerable computational burden. For this reason, available computational models tend to make a compromise between capturing the discharge chemistry, by including a large number of species; or, by capturing the discharge physics by including fewer chemical species but simulating more realistic geometries. For example, Sakiyama *et al.* built two coupled 0D models to examine the

chemistry in an SMD discharge [16], where the first model followed the averaged densities of short-lived (including charged species) and long-lived species in the vicinity of the driven electrode, while the second model followed only the averaged densities of the long-lived species in the afterglow region, which is a region extending 10 mm away from the electrodes. It was reported that out of the 53 species included in the model, only 9 species have a significant density in the afterglow region, and that the densities of these species are still changing in time after 1000 seconds. Liu *et al.* extended the model Sakiyama *et al.* developed by replacing the 0D model in the afterglow region with a 1D model and adding a further 1D model to describe the chemistry in a water layer placed downstream of the electrode [18]. They showed that many of the chemically active species in water such as OH, HO_2, and O_2^- are generated locally through reactions between the long-lived species generated by the plasma and the molecules of the liquid.

In this work, we merge the two models used in [16, 18] into a single 1D reaction-diffusion model. Furthermore, we take convection into account on time scales much longer than the period of the assumed waveform. This is critical, given that the electrohydrodynamic force in an SBD configuration is known to induce flow velocities up to several m/s around the electrode structure [19,20]; which is found to be a more significant mechanism of species transport than diffusion, which is the only mechanism considered in previous models [16,18]. In addition, we investigate the impact of the applied power on the chemistry of the discharge by solving the model for three different powers.

2. Numerical model

The discharge configuration simulated in this work is a SBD operating in ambient air. It is similar to the discharges used as plasma based actuators [21]. The configuration assumed is representative of a typical SBD where many parallel conductors are placed on a dielectric surface, creating ‘trenches’ where the plasma is generated as filamentary discharges having a life-time of few tens of nanoseconds in every cycle of the applied waveform. A schematic diagram of the discharge configuration is shown in figure 1. Plasma is assumed to form in the trench between the driven electrodes, designated in

figure 1(a) as the hashed zone. The dimensions of this zone are 40 μm by 2 mm. by 646 mm in the third dimension.

2.1 Model implementation

The model used here is a 1D time-dependant model. The computational domain is depicted in figure 1(a) as the vertical line extending from the hatched zone above the dielectric. It extends from the surface of the dielectric (where the active plasma region is) up to 10 cm. The model was implemented using COMSOL and consists of a coupled system of reaction-diffusion equations (convection is considered only on long time scales). It follows the densities of 53 species including electrons, ions, and neutrals. The chemical species and reaction considered in the model are the same as those reported in [16].

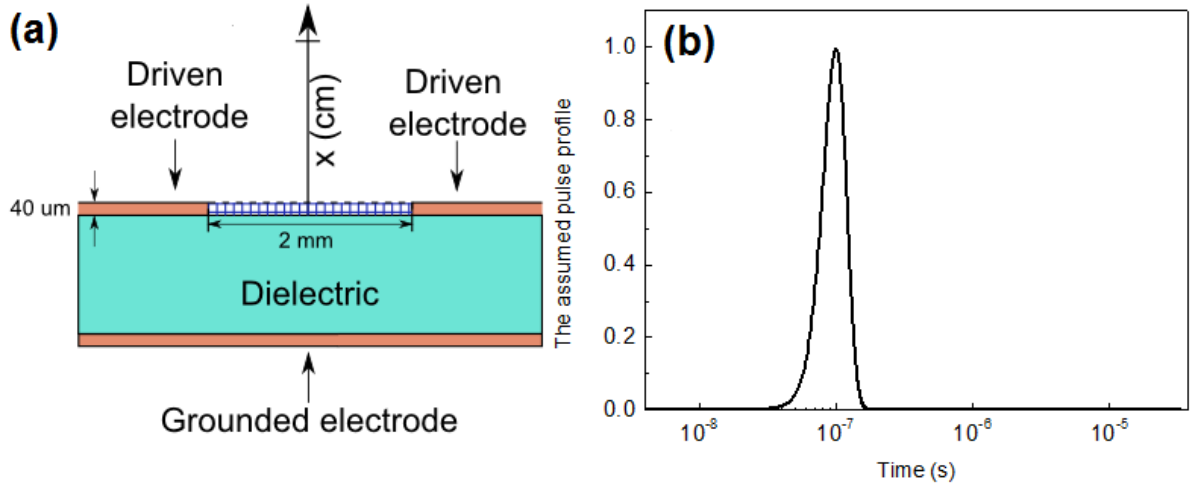

Figure 1. A schematic diagram showing a cross section of the discharge configuration is shown in (a), the hatched zone is where the plasma is generated. The vertical line pointing upwards represents the computational domain used in this work, (b) the time profile of the applied pulse assumed in the model.

The densities of all species except electrons are determined using equation (1). This equation is solved for the mass fraction ω_j (dimensionless) of the j^{th} species.

$$\rho \frac{\partial \omega_j}{\partial t} - \nabla \cdot \left(D_j \frac{\rho}{M_n} \nabla \left(M_n \omega_j \right) \right) = M_j R_j \qquad (1)$$

where ρ (kg.m^{-3}) is the density of air set equal to 1.19, D_j (m^{2}s^{-1}) is the diffusion coefficient of the j^{th} species, M_n (kg.mol^{-1}) is the mean molecular weight of the mixture, M_j (kg.mol^{-1}) is the molecular weight of the j^{th} species, and R_j (mol.m^{-3}s^{-1}) is the generation or loss rate of the j^{th} species due to chemical reactions. Diffusion coefficients for all species except electrons are taken from [16]. The electron reaction-diffusion equation is solved in terms of the number density n_e (m^{-3}), which is given by equation (2).

$$\frac{\partial n_e}{\partial t} - \nabla \cdot \left(D_e \nabla n_e \right) = R_e \tag{2}$$

where D_e (m^{2}s^{-1}) is the diffusion coefficient of electrons and R_e (m^{-3}s^{-1}) is the electron generation or loss rate due to chemical reactions. Many of the chemical reactions involving electrons as a reactant have reaction coefficients that depend on the mean electron energy. To obtain the electron temperature, the local field approximation is assumed. Using BOLSIG+ [22] and the cross sections of N_2, O_2, and H_2O are obtained from the Morgan database [23], the electron energy distribution function (EEDF) is computed for different values of the reduced electric field, then the mean electron energy is computed from the EEDF, giving the mean electron energy as a function of the reduced the electric field. In addition, the electron mobility μ_e and their diffusion coefficient D_e (m^{2}s^{-1}) is obtained from BOLSIG+ as functions of the mean electron energy.

The model does not solve for the electric potential or the electric field, as the electrodes are outside the computational domain. Instead, the driving electric field (and consequently the reduced electric field) is assumed to be a Gaussian pulse in time, representing a filamentary discharge. This pulse is described mathematically in equation (3), the temporal profile of the pulse is shown in figure 1(b).

$$E_N = \frac{E_0}{N} \exp\left(-\frac{1}{2}\left(\frac{t - 5\tau_p}{\tau_p} \right)^2 \right) \tag{3}$$

where E_N (Vm^2) is the reduced electric field, N (m^{-3}) is the number density of particles at ambient conditions, set to 2.5×10^{25}, t (s) is time, τ_p (s) is the filamentary discharge duration set to 20 ns, and E_0 (Vm^{-1}) is a pre-set value of the electric field chosen to match the deposited power in the discharge.

As the electric field is computed, the equivalent mean electron energy is evaluated. Since the electrons are not expected to have any energy above the thermal energy at room temperature outside the hatched zone shown in figure 1, a decaying exponential profile is multiplied by the mean electron energy, such that the mean electron energy beyond 0.1 mm above the dielectric surface is equal to the thermal energy at room temperature.

2.2 Model operation

The model is run in two stages, a short stage and a long stage. A flow diagram of the model is shown in figure 2. In the short stage, the model is solved for multiple consecutive time periods corresponding to a frequency of operation of 30 kHz. After one period is computed, the computed power deposited in the discharge is determined using equation (4). By comparing the computed power to the set power, a correction in the value of the assumed electric field E_0 is added to minimize the difference between the computed power and the set power. The value of this correction is given by equation (5). The simulation is run until four consecutive periods have a computed power deviating by less than 5% of the set power. During these four periods, the value of E_0 is held constant. This marks the end of the short stage of the model.

$$P_{comp} = \frac{q_e h}{\tau_p} \int_{\tau_p} \sum_j \mu_j n_j |E|^2 \, dt \tag{4}$$

$$\Delta E_0 = \alpha (P_{set} - P_{comp}) \tag{5}$$

where q_e (C) is the electron charge, h is the height of the anode set to 40 μm, n_j and μ_j are the number density and the mobility of the j^{th} species. The mobilities of all ions are computed from their diffusion coefficients using Einstein's relation [24]. The summation in equation (4) runs over charged species only. Equation (4) is evaluated at the boundary x = 0, which corresponds to the trench where the

plasma is created. In equation (5), ΔE_0 is the correction of the assumed electric field to match the computed power P_{comp} to the set power P_{set}, and α is a feedback parameter.

During the last solved period of the short stage simulation, the generation rates of neutral species are integrated in time, and then divided by the period giving their time-averaged generation rates. These are then used as inputs to the long stage of the model, where only the densities of neutral species are solved for. The long stage is solved for 10 seconds without resolving the waveform periods in time, as their effect is accounted for by the time—averaged generation rates obtained from the short stage of the model. This coupling between the short stage and the long stage of the model is known as one-way coupling [a], which has lower accuracy compared to other schemes but shorter computation times. The short stage phase of the model presented here takes approximately a week running time. For this reason, other coupling schemes involving continuous re-computation of the short stage phase are impractical. Since the long stage phase of the model is only solved for 10 seconds, it is expected that the difference between the different coupling schemes will be small.

The equations solved in the long stage of the model are the same as the short model, except that a mechanical convection term is added to equation (1), where the species are carried away by the flowing background at assumed uniform velocity field. The assumption of a uniform velocity field is a simplification of complex flow structure observed in experiments, which is done to suit the 1D nature of the model described in this work. It should be noted that because mechanical convection is completely ignored during the short stage of the model, the model is limited to low flow rates (< 1 ms^{-1}).

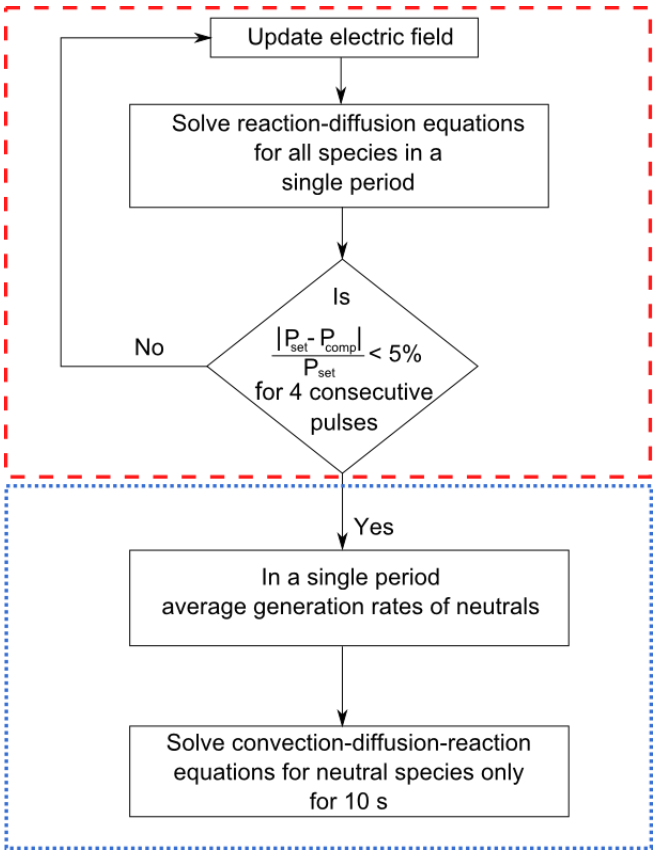

Figure 2. A flow diagram of the model, the part enclosed by the dashed red box is the short stage, and the part enclosed by the dotted blue box is the long stage of the model.

3. Results and discussion

The model is solved for three powers, which are 5 W, 10 W, and 15 W, chosen to match on-going experimental investigations. These powers are converted into power densities by dividing them by the volume of the trench shown in figure 1, giving power densities of 0.387, 0.774, and 1.16 ($W.cm^{-2}$) for 5, 10, and 15 W cases respectively. It should be noted here that the area used here to convert the power into a power density is less than that used in [16] and similar works, which is the total electrode area. Using the total electrode area as the conversion factor gives a power density of approximately 0.1 ($W.cm^{-2}$) for 15 W case, which is the upper limit of the power domain in which the chemical model is valid [16].

For the three cases, the model required approximately 200 periods to satisfy the power constraint. After that, the long stage of the model is run assuming three flow velocities, 0, 0.1, and 0.3 ms^{-1}. All the figures shown in this section are for the 10 W case unless stated otherwise.

Experimental evaluation of the validly of the model is difficult, as most experimental techniques do not provide quantitative information on the available species. Instead, to assess the validity of our model, the conditions reported by Sakiyama *et al.* were implemented in our model to provide a comparison with the results reported therein. Figure 3 shows a comparison between some of the results obtained using our model and these reported in [16].

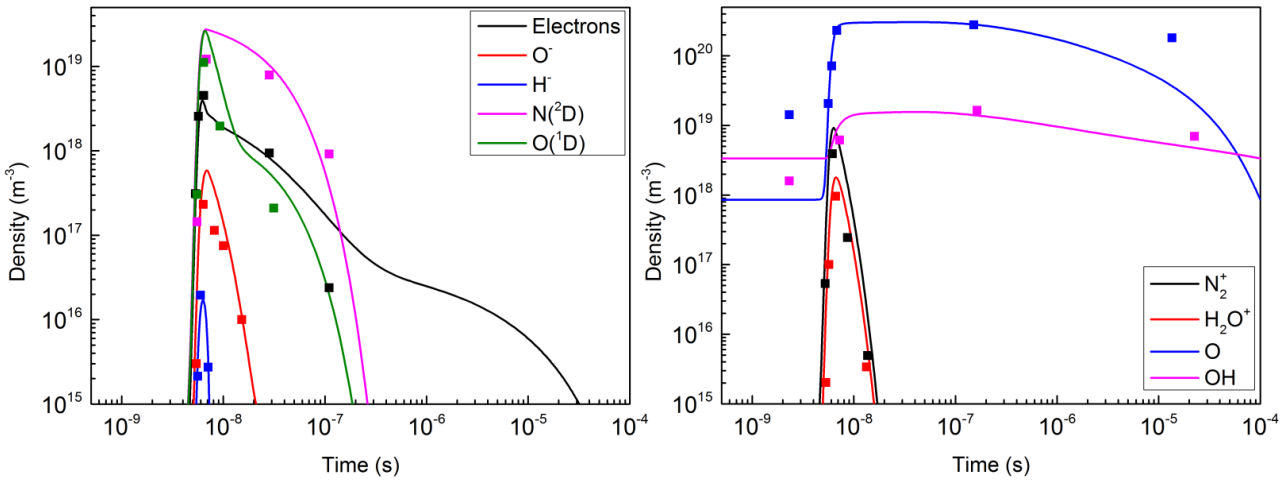

Figure 3. A comparison of the densities of selected set of species between the results obtained using the model presented here (solid lines) and the model reported in [16] (square points).

It is shown in figure 3 that the results are in good agreement. It should be noted that the structure of the model presented here is different in comparison with [16]. For this reason, it is expected that there are some minor differences in the densities. The densities shown in figure 3 are computed using the short stage of the model only. The long stage part of the model was not run for this case.

As the number of species studied on different time scales is large, the behaviour of selected key species is discussed. These species are chosen to represent general behaviour followed by the other species.

3.1 Charged species

The behaviour of the charged species is only discussed for the short stage of the model. As soon as the pulse is applied, the mean electron energy increases, initiating ionization reactions which generate predominately N_2^+ ions. Later during the pulse, the initial N_2^+ ions and electrons undergo further reactions, generating many other positive and negative ions species such as H_3O^+, O_2^+, O_2^-, and O_3^-. After the pulse ends, the mean electron energy drops, increasing the density of negative ions and creating new species such as O_4^- and NO_2^-. Figure 4 shows the major reaction pathways of the ionic species as a function of time. Each specie is located in the time interval where its density peaks at *x = 0* (*i.e.* at the dielectric). A list of the chemical reactions listed in figure 4 can be found in the appendix. These reactions are a subset of the main reaction set implemented in the model, consisting of 624 reactions listed in [16].

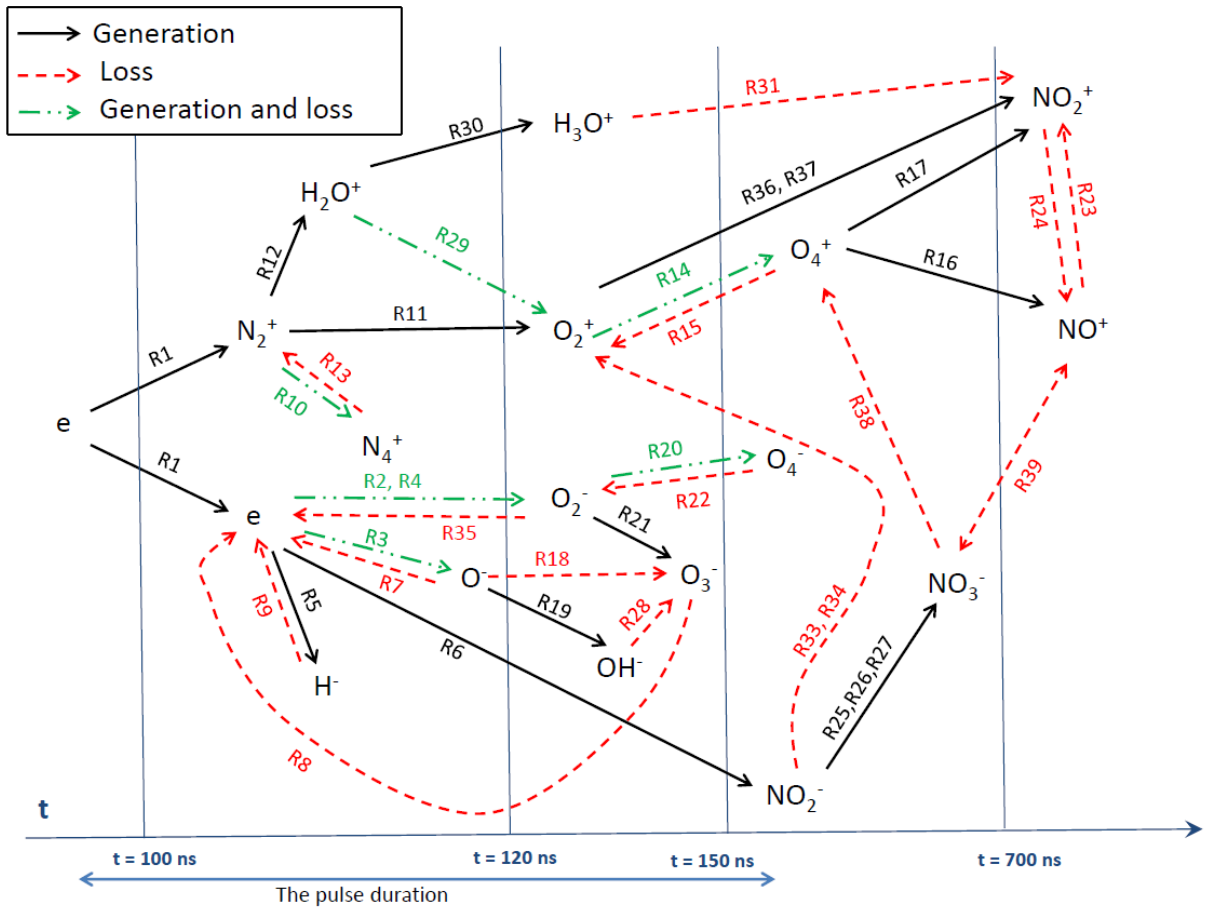

Figure 4. Time evolution diagram of the ionic species with respect to the applied pulse. Each species is located in the time interval where it density peaks at x = 0. Black solid arrows represent the major generation reaction of the species at the end of the arrow. Red dashed arrows represent the major loss reaction of the species at the beginning of the arrow. Green dashed and dotted arrows represent the major generation reaction of the species at the end of the arrow and the major loss reaction at the beginning of the arrow.

The spatial distribution of the ionic species, shown in figure 5, indicates that the density of the positive ions decay sharply as one moves away from the dielectric surface (*i.e. x = 0 cm* point), while the negative ions densities and the electrons have a more gradual decay in comparison. To highlight this behaviour, figure 5 shows the densities of 4 selected species which are the electrons, O_2^-, N_2^+, and NO^+ as a function of position (*x*) at two different times. It is clear that the positive ions densities in figure 5 drop by almost one order of magnitude within 10 μm of the dielectric surface, compared to the electrons and the O_2^- ions which drop by the same factor within 100 μm of the dielectric surface. The reason for this difference stems from the fact that the main positive ion from which many others form is N_2^+ as indicated by figure 4. The main generation reaction of N_2^+ is electron impact ionization, which has a rate coefficient depending on the mean electron energy. This makes the spatial distribution of N_2^+ strongly correlated with the spatial distribution of the mean electron energy. Other positive ionic species follow the distribution of N_2^+ as they are indirectly generated from it as shown in figure 4. The density of N_2^+ drops in time by more than an order of magnitude within 130 ns, while the density of NO^+ increases by a similar factor within the same time, as highlighted by figure 5. This is a consequence of the 'sequential' generation of ionic species in a single period. Most other positive ionic species have a similar spatial distribution to N_2^+.

With respect to the electrons, the reason behind their spatial spread is their high diffusion coefficient in comparison with ions. The electron diffusion coefficient increases as the mean electron energy increases during the pulse, causing electrons to spread spatially. After the pulse is switched-off, the mean electron energy decreases causing the diffusion of electrons to reduce. The initial rapid diffusion

followed by the subsequent slow diffusion causes the gradual drop in the density seen in figure 5. With respect to the O_2^- ions, figure 4 shows that they are mainly generated through two and three body attachment of electrons to O_2 molecules, which means that the spatial distribution of the O_2^- ions density is strongly correlated with the electron density. The slower drop in the density of O_2^- ions is a consequence of the slower drop in electron density as a result of the diffusion of the electrons.

Figure 5 also shows that the electron density declines by approximately an order of magnitude within 130 ns, while the density of the O_2^- ions increases by a factor of 2. This increase is also attributed to the sequential generation of the ionic species in a single period. Most other negative ionic species have a similar spatial distribution as that of O_2^-.

It should be noted that the difference in the spatial spread between the positively charged and negatively charged species is expected to be less than shown in figure 5 due to ambipolar diffusion, which has not been accounted for in this model.

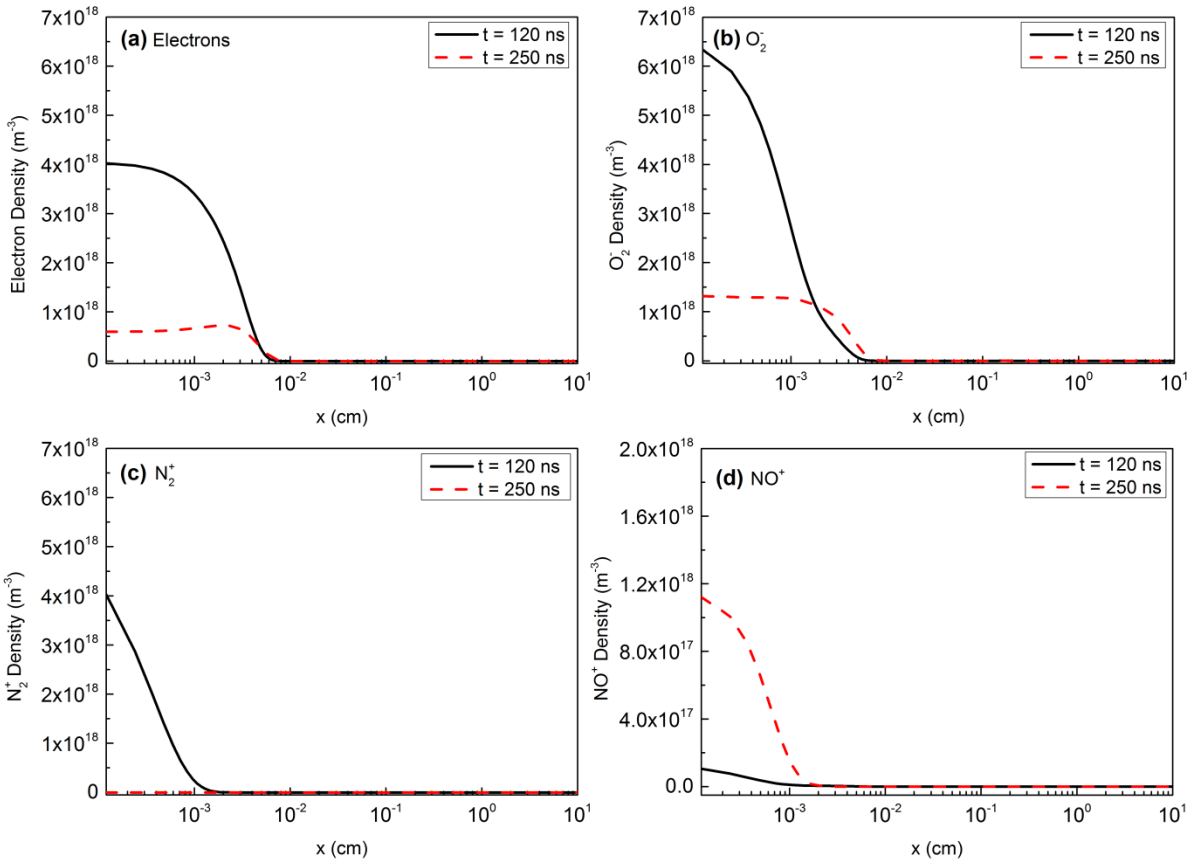

Figure 5. The density of (a) the electrons, (b) O_2^- *ions, (c)* N_2^+ *, and(d)* NO^+*. All densities are shown at 120 ns and 250 ns. All panels have the same scale except (d). In this figure, t = 0 represents the beginning of the last solved period of the short stage of the model.*

3.2 Neutral species

Unlike the charges species, the temporal behaviour of the neutral species varies widely. In general, neutral species can be categorized based on their temporal behaviour into three categories. A category named short-lived species; which are generated and destroyed within a single period of the applied voltage waveform, similar to the charged species. Examples of these are $N_2(A^3\Pi)$, $N(^2D)$, and $O(^1D)$. The second category contains species where the density increases during the pulse-on time, but the drop in density after the pulse is removed is slower than the generation, which means there is a net accumulation in the density over a period of the waveform. These species can be called intermediate-lived species such as OH, $O_2(a^1\Delta)$, and N. The life-time of these species is comparable to the period of the applied waveform.

The third category contains species that have no appreciable change during a period of the waveform. However, their density grows over a large number of periods. These species can be called long-lived species. Examples include O_3, HNO_3, and NO_2.

With respect to the spatial distribution, the densities of the neutral species can be divided into a either a wide distribution, similar to that of negative ions, or a narrow distribution, similar to that of the positive ions, as described in section 3.1. To show this, 4 species are selected and plotted as a function of position (x) in figure 6 at two time points. It shows that the OH and N densities have wide distributions at t = 0, while the 'added' densities as a result of the applied pulse (in figures 6(a) and (c)) have narrow spatial distributions. This is a consequence of the accumulation of OH and N which allows them to experience diffusion, causing the density to spread in space and giving them a wide distribution. Other species with similar behaviour to OH and N include O and $O_2(a^1\Delta)$, which are key antimicrobial agents. Short-lived species however, such as $O(^1D)$ and $N_2(A^3\Sigma)$ do not live long enough to experience diffusion, as they are lost through rapid reactions, which means their spatial

distribution is strongly correlated with that of the energetic electrons during the pulse-on time, being a narrow distribution. Other species with similar behaviour to $O(^1D)$ and $N_2(A^3\Sigma)$ include $N(^2D)$, $N_2(B^3\Pi)$, and H.

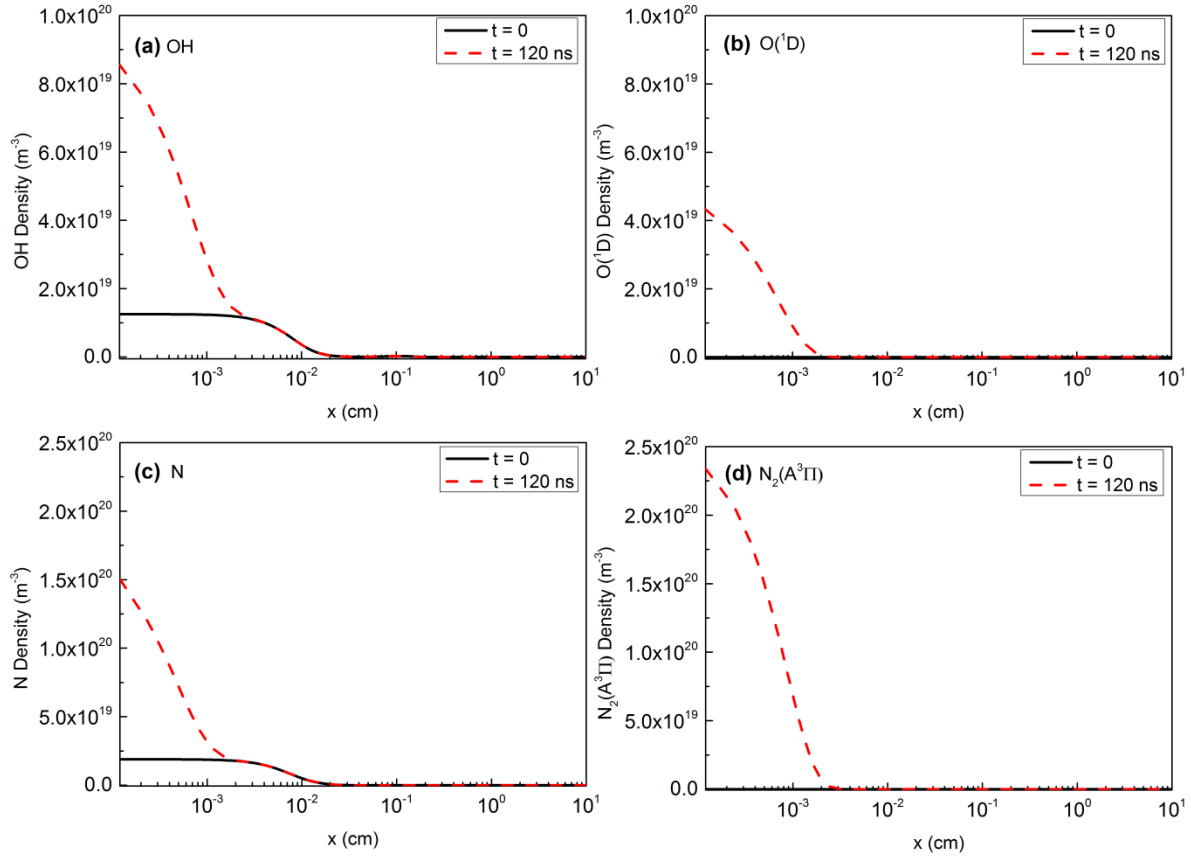

Figure 6. The density of (a) OH, (b) $O(^1D)$, (c) N, and (d) $N_2(A^3\Pi)$. All panels shows the densities at t = 0 and t = 120 ns. Panels (a) and (b) have the same scale, so do (c) and (d). In this figure, t = 0 represents the beginning of the last solved period of the short stage of the model.

It can be seen from figure 6 that the densities of OH and N at *t = 0* are much greater than zero, which indicates that this density is an accumulation from previous pulses. Since these two species are highly reactive, their accumulation indicates that their life-time is longer than the period of the assumed waveform of 30 kHz, thus they can be described as intermediate-lived species. The densities of $O(^1D)$ and $N_2(A^3\Pi)$ however start from almost zero, indicating they are short-lived species. It is also worth pointing out that long-lived species, including O_3, N_2O_5, NO, N_2O, NO_2, NO_3, HNO_3, HO_2, H_2O_2, and HNO_2, are not shown as their density varies little over the duration of a single pulse.

3.3 Long stage simulation

Based on the behaviour of the charged and neutral species in the short stage of the model, only the intermediate-lived and long-lived species are solved in the long term stage of the model, their generation rate is averaged over the last pulse of the short stage, and then the chemical reactions involving short-lived species are deactivated. Figure 7 shows the spatial distribution of selected species at different times for an applied power of 10 W and no convection.

It is shown in figure 7 that all the species plotted start at a high density close to the dielectric surface, and then gradually move by diffusion further downstream of the electrode, which can be clearly seen from the spatial profiles of O_3, HNO_3, and NO_2. The density of O_3 increases slowly away from the dielectric surface, this increase in the density is attributed to the reaction $O + O_2 + M \rightarrow O_3 + M$ although the density of O in that region is in the order of 10^{13} m^{-3}, this increase in the density is insignificant compared to the density increase due to the diffusion from the dielectric surface. Similarly, the density of HNO_3 increases slowly away from the dielectric surface as a result of the reaction $OH + NO_2 + M \rightarrow M + HNO_3$, this reaction is also responsible for rapid decay of the OH density away from the electrode as it is one of the main loss reactions of OH.

Another observation from figure 7 is that the densities of the plotted species slightly change at the point $x = 0$ (at the dielectric surface) as a function of time. This variation eventually diminishes to a steady state value. The maximum change of density is for O_3, where the density at the dielectric surface has increased by almost a factor of 3 over 10 s. the density of HNO_3 at the same point has increased by 10%, while there is no increase in the density of NO_2 at the same location.

Most species not plotted in figure 7 exhibit a similar behaviour to O_3, where their density increases everywhere as a result of diffusion from the surface of the dielectric. Some other species such as OH N, O, NO, HO_2 and $O_2(a^1\Delta)$ have different behaviour, where their densities drop rapidly away from the dielectric surface as they are converted by chemical reactions into long-lived species. It should be noted that all the previously mentioned species (OH etc.) are intermediate-lived species.

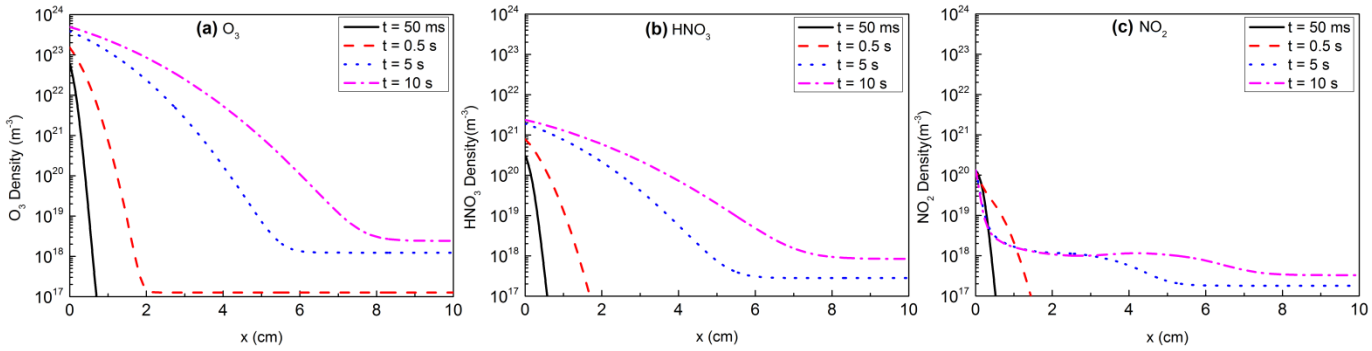

Figure 7. The densities of (a) O_3,(b) HNO_3, and (c) NO_2 as functions of space at t= 0.5 ms, 0.5 s, 5 s, and 10 s. All panels have the same scale.

3.4 The effect of convection

The long stage part of the model is solved for three convection velocities, 0, 0.1 $m.s^{-1}$, and 0.3 $m.s^{-1}$. A comparison of the spatial distribution of O_3 and NO_2 for the different flow rates is shown in figure 8.

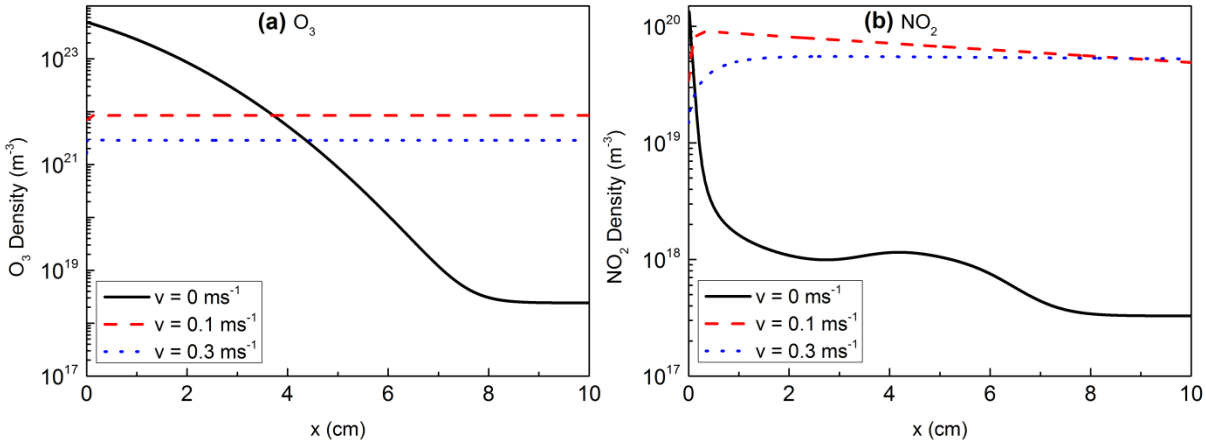

Figure 8. The density as function of space at 10 s of (a) O_3 and (b) NO_2. The densities for the no flow case are shown in solid black, the densities of a flow velocity of 0.1 ms^{-1} are shown in dashed red, and the densities for a flow velocity of 0.3 ms^{-1} are shown in dotted blue.

It is clear from figure 8 that convection increases the uniformity of the spatial distribution of long-lived plasma generated species in the gas phase. Given that convection is inevitable in the SBD configuration, it is clear that this process is the dominant mechanisms driving the transport of plasma species from the plasma region in to the downstream gas. The convection causes the O_3 density to drop compared to the no convection case close to the dielectric surface, while the O_3 density increases

away from the dielectric surface. Convection in such a case serves as a means of mass transport by moving O_3 molecules from a zone where the density is high, causing the local density to drop, to a zone with lower density causing it to rise, the total O_3 density in the computational domain is decreased as a result of the convective flux leaving the computational domain. Other species with similar behaviour to O_3 include: H_2O_2, HNO_2, NO_3, and N_2O. For these species, convection has a stronger influence on their spatial distribution than the change in their chemical reaction rates as a result of the new distribution.

With respect to NO_2 density, figure 8 shows that the convection causes an increase everywhere. For NO_2, the change in the chemical reaction rate as a result of the convection has a stronger influence than convection itself. Furthermore, in the first few microseconds of the simulation the main loss reaction of NO_2 is $NO_2 + OH + M \rightarrow HNO_3 + M$. The main impact of convection on NO_2 density is that it reduces the residence time of NO_2 in the region where the density of OH is high (close to the dielectric surface), hence minimizing the effect of the main loss reaction and allowing greater numbers of NO_2 molecules to spread spatially. It should be noted that convection has no significant impact on OH density because it is highly reactive and is quickly lost in reactions with other species.

3.5 The effect of applied power

Intuitively, an increase in the applied power will increase the mean electron energy during the pulse, which will generate more electrons and cause a greater activation of the chemistry in air. Critically, an increase in the electron density and mean energy does not necessarily mean that all species will follow the same trend. The O_2^- density, for example, is shown in figure 9 at different locations as a function of time. From the figure it is clear that the higher the power is, the higher the maximum density is, which is expected as a result of having more electrons available for attachment when the pulse is switched-off. The peak O_2^- density in the 5 W case is 3.7×10^{18} (m^{-3}), while for the 10 W it is 6.8×10^{18} and 1×10^{19} for the 15 W case. In this case, the increase in peak density is approximately proportional to the increase of the power. Most of the other ionic and excited species generated in the pulse also follow this proportionality with applied power.

Figure 9 also shows that the time-decay of the O_2^- density in the 5 W case is slower than the other two cases; the reason for this difference can be explained by the reaction $O_2^- + O_3 \rightarrow O_3 + O_2 + e$, which is one of the main loss reactions of O_2^-. Examining the O_3 density, the simulation shows that the O_3 density for the 5 W case is 9×10^{21} (m^{-3}) compared to 5.2×10^{22} and 4.8×10^{22} for the 10 W case and the 15 W respectively. As a result, the reaction is much stronger in 10 W and 15 W cases. Other ionic species that have a slower decay in time in the 5W case compared to the other two cases are OH^-, O_2^-, and O_4^-.

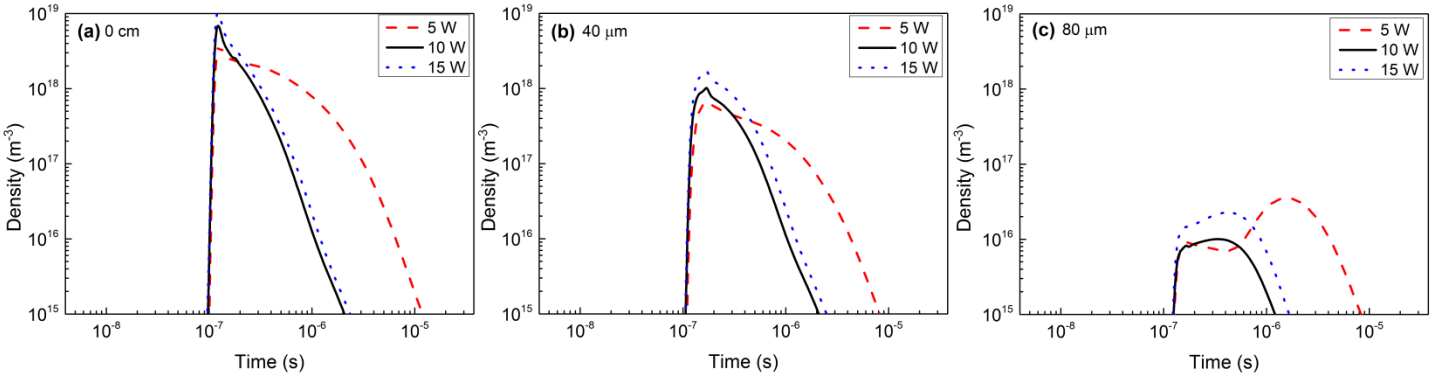

Figure 9 The O_2^- density as function of time at (a) x = 0 cm, (b) x = 40 μm, and (c) x = 80 μm. The dashed red line represents the 5 W power case, the solid black line represents the 10 W power case, and the dotted blue line represents the 15 W power case.

With respect to neutral species densities, only species from the long stage part of the model are considered here. An increase in power causes a variant increase in the density of the generated species. For example, the maximum density of O_3 at the dielectric surface (refer to figure 7) increases in the no convection case from 2×10^{23} (m^{-3}) for 5 W case to 4×10^{23} and 6×10^{23} for 10 W and 15 W respectively at 10 s. While for NO_2, the increase for the no convection case occurs from 8×10^{19} (m^{-3}) for the 5 W case to 1.3×10^{20} and 1.6×10^{20} for the 10 W and the 15 W cases respectively. For cases where convection is included, the spatial distribution is almost a straight line along the domain as discussed in section 3.4 (refer to figure 8). The densities of O_3 and NO_2 for different powers and flow velocities are shown in figure 10. It is clear that the densities for the 0.3 ms^{-1} are slightly lower

compared to those for the 0.1 ms^{-1} as a result of the stronger convective flux. The densities in the figure show that the proportionality with power holds for both flow velocities.

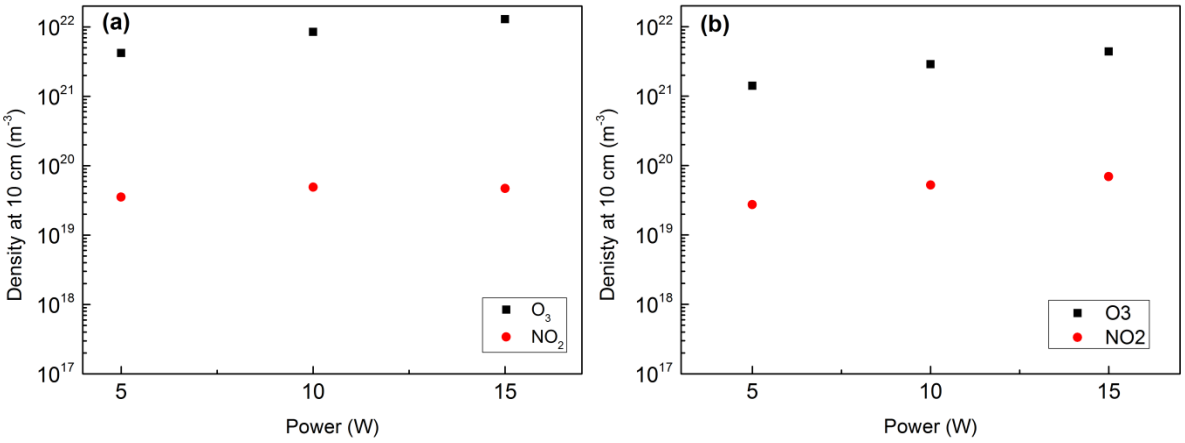

Figure 10: Densities of O_3 and NO_2 at x = 10 cm for flow velocity of (a) 0.1 ms^{-1} and (b) 0.3 ms^{-1}. Data obtained at t = 10 s.

4. Conclusions

In this work, the spatial and temporal behaviour of chemical species generated in air SBD discharge are investigated using a 1D computational model. The study focused on the chemistry produced by the discharge over both short (a period of the applied voltage waveform) and long-time scales (up to 10 seconds). The impact on the discharge chemistry of varying the applied discharge power and introducing a realistic convective flow was investigated.

It was demonstrated that charged species are generated and destroyed within one period of the applied waveform; different positive and negative ions are generated sequentially, with simple ions such as N_2^+ and O_2^- being generated at around the maximum field value, and are then subsequently converted through chemical reactions into other ions such as NO_3^- and NO^+. The spatial distribution of the negative ions is wider than that of the positive ions, which is a result of the electrons diffusing away from the dielectric to regions where they are lost in attachment reactions.

The neutral species in the discharge are categorized based on their temporal behaviour into three categories which are: short-lived species, intermediate-lived species and long-lived species. Short-

lived species are generated and destroyed in a single period of the applied waveform; thus they have life-times smaller than the period of the applied waveform. Their spatial distribution resembles that of electrons, with most of the species in this category being electronically excited states such as $N_2(A^3\Pi)$ and $O(^1D)$. The second category is the intermediate-lived species. Species in this category such as OH and N have life-times comparable to the duration of the applied waveform, which allows them to accumulate over many periods. Their spatial distribution is wider than that of the electrons due to the fact that their accumulated density lives long enough to experience diffusion. The third category is the long lived species, which includes O_3, NO_2, H_2O_2 and many other species. In this category are species that have much longer life-times than the period of the applied waveform. The densities of these species barely changes during a period of the applied waveform. Their spatial distribution is very wide, filling the whole simulation domain even in the absence of convection.

The impact of mechanical convection on most species (long-lived species) is that it makes their spatial distribution uniform compared to the no convection case (over the duration of the simulation $t = 10\ s$). Convection causes a drop in the density for most species, as it removes them out of the computational domain, preventing accumulation of the species next to the surface of the configuration. An exception is NO_2, where convection causes an increase in density. This happens as the residence time of NO_2 close to the dielectric surface (where it is lost in reactions with OH) is reduced, causing NO_2 molecules to live longer.

The densities of the charged species and the neutral species in the three categories are found to proportional to the applied power to the discharge.

Acknowledgement

The authors would like to thank InnovateUK for supporting this work financially under grant number 102318.

Appendix

In this appendix, the list of the reactions depicted in figure 3 is given.

No	Reaction	No	Reaction
R1	$e + N_2 \rightarrow 2e + N_2^+$	R21	$O_2^- + O_3 \rightarrow O_3^- + O_2$
R2	$e + 2O_2 \rightarrow O_2 + O_2^-$	R22	$O_4^- + N_2 \rightarrow O_2^- + O_2 + N_2$
R3	$e + O_2 \rightarrow O + O^-$	R23	$N_2O_5 + NO^+ \rightarrow 2NO_2 + NO_2^+$
R4	$e + O_2 \rightarrow O_2^-$	R24	$NO + NO_2^+ \rightarrow NO_2 + NO^+$
R5	$e + H_2O \rightarrow OH + H^-$	R25	$NO_2 + NO_2^- \rightarrow NO + NO_3^-$
R6	$e + HNO_3 \rightarrow OH + NO_2^-$	R26	$O_3 + NO_2^- \rightarrow O_2 + NO_3^-$
R7	$O^- + O_3 \rightarrow 2O_2 + e$	R27	$HNO_3 + NO_2^- \rightarrow HNO_2 + NO_3^-$
R8	$O_3^- + O_2 \rightarrow O_3 + O_2 + e$	R28	$O_3 + OH^- \rightarrow OH + O_3^-$
R9	$H^- + O_2 \rightarrow HO_2 + e$	R29	$O_2 + H_2O^+ \rightarrow O_2^+ + H_2O$
R10	$N_2^+ + N_2 + M \rightarrow M + N_4^+$	R30	$H_2 + H_2O^+ \rightarrow H + H_3O^+$
R11	$N_2^+ + O_2 \rightarrow N_2 + O_2^+$	R31	$N_2O_5 + H_3O^+ \rightarrow HNO_3 + H_2O + NO_2^+$
R12	$N_2^+ + H_2O \rightarrow N_2 + H_2O^+$	R32	$O_2^+ + O_3^- \rightarrow O_3 + O_2$
R13	$N_4^+ + N_2 \rightarrow 2N_2 + N_2^+$	R33	$O_2^+ + NO_2^- \rightarrow NO_2 + O_2$
R14	$O_2^+ + O_2 + M \rightarrow M + O_4^+$	R34	$O_2^+ + NO_2^- \rightarrow NO_2 + 2O$
R15	$O_4^+ + O \rightarrow O_3 + O_2^+$	R35	$O_2^- + O_3 \rightarrow O_3 + O_2 + e$
R16	$O_4^+ + NO \rightarrow 2O_2 + NO^+$	R36	$N_2O_5 + O_2^+ \rightarrow NO_3 + O_2 + NO_2^+$
R17	$O_4^+ + NO_2 \rightarrow 2O_2 + NO_2^+$	R37	$NO_2 + O_2^+ \rightarrow O_2 + NO_2^+$
R18	$O^- + O_2 + M \rightarrow O_3^- + M$	R38	$O_4^+ + NO_3^- \rightarrow 2O_2 + NO_3$
R19	$O^- + H_2O \rightarrow OH + OH^-$	R39	$NO^+ + NO_3^- \rightarrow N + O + NO_3$
R20	$O_2^- + O_2 + M \rightarrow O_4^- + M$		

Table A1. A list of the reactions referred to in figure 4. All the rate coefficients of these reactions are taken from [16].

References

[1] G. Y. Park, S. J. Park, M. Y. Choi, I. G. Koo, J. H. Byun, J. W. Hong, J. Y. Sim, G. J. Collins and J. K. Lee, "Atmospheric-pressure plasma sources for biomedical applications" *Plasma Sources Sci. Technol.* **21** 043001 (2012) doi:10.1088/0963-0252/21/4/043001

[2] K.-D. Weltmann, K. Fricke, M. Stieber, R. Brandenburg, T. von Woedtke, and U. Schnabel, "New Nonthermal Atmospheric-Pressure Plasma Sources for Decontamination of Human Extremities" *IEEE Trans. Plasma Sci.* **40** 2963 (2012) doi: 10.1109/TPS.2012.2204279

[3] M. D. G. Evans, F. P. Sainct, F. Aristizabal, J. M. Bergthorson , S. Coulombe "Development of a nanosecond pulsed HV atmospheric pressure plasma source: preliminary assessment of its electrical characteristics and degree of thermal nonequilibrium*" J. Phys. D: Appl. Phys.* **48** 255203 (2015) doi:10.1088/0022-3727/48/25/255203

[4] J. Ehlbeck, U. Schnabel, M. Polak, J. Winter, T. von Woedtke, R. Brandenburg, T. von dem Hagen and K.-D. Weltmann "Low temperature atmospheric pressure plasma sources for microbial decontamination" *J. Phys. D: Appl. Phys.* **44** 013002 (2011) doi:10.1088/0022-3727/44/1/013002

[5] D. B. Graves "The emerging role of reactive oxygen and nitrogen species in redox biology and some implications for plasma applications to medicine and biology" *J. Phys. D: Appl. Phys.* **45** 263001 (2012) doi:10.1088/0022-3727/45/26/263001

[6] M. J. Kirkpatrick, B. Dodet and E. Odic "Atmospheric Pressure Humid Argon DBD Plasma for the Application of Sterilization - Measurement and Simulation of Hydrogen, Oxygen, and Hydrogen Peroxide Formation" *Int. J. Plasma Environ. Sci. Technol.* **1** 96 (2007)

[7] P. Muranyi, J. Wunderlich, M. Heise "Influence of relative gas humidity on the inactivation efficiency of a low temperature gas plasma" *J. Appl. Microbiol.* **104** 1659 (2008) doi:10.1111/j.1365-2672.2007.03691.x

[8] G. Isbary, G. Morfill, J. Zimmermann, T. Shimizu, W. Stolz "Cold Atmospheric Plasma A Successful Treatment of Lesions in Hailey-Hailey Disease" *Arch Dermatol.* **4** 388 (2011) doi:10.1001/archdermatol.2011.57.

[9] G. Isbary, J. Heinlin, T. Shimizu, J. L. Zimmermann, G. Morfill, H.-U. Schmidt, R. Monetti, B. Steffes, W. Bunk, Y. Li, T. Klaempfl, S. Karrer,M. Landthaler and W. Stolz "Successful and safe use of 2 min cold atmospheric argon plasma in chronic wounds: results of a randomized controlled trial" *British Journal of Dermatology* **167** 404 (2012) doi 10.1111/j.1365-2133.2012.10923.x

[10] A. N. Idlibi, F. Al-Marrawi, M. Hannig, A. Lehmann, A. Rueppell, A. Schindler, H. Jentsch, S. Rupf "Destruction of oral biofilms formed *in situ* on machined titanium (Ti) surfaces by cold atmospheric plasma" *The Journal of Bioadhesion and Biofilm Research* **29** 369 (2013) doi: 10.1080/08927014.2013.775255

[11] I. Koban, B. Holtfreter, N.-O. Hübner, R. Matthes, R. Sietmann, E. Kindel, K.-D. Weltmann, A. Welk, A. Kramer, T. Kocher "Antimicrobial efficacy of non-thermal plasma in comparison to chlorhexidine against dental biofilms on titanium discs in vitro – proof of principle experiment" *Journal of Clinical Periodontology* **38** 956 (2011) doi**:** 10.1111/j.1600-051X.2011.01740.x

[12] K. R. Stalder, D. F. McMillen, J. Woloszko "Electrosurgical plasmas" *J. Phys. D Appl. Phys.* **38** 1728 (2005) doi:10.1088/0022-3727/38/11/014

[13] E. Stoffels, I. E. Kieft and R. E. J. Sladek "Superficial treatment of mammalian cells using plasma needle" *J. Phys. D: Appl. Phys.* **36** 2908 (2003)

[14] T. Shimizu, J. L. Zimmermann, G E Morfill "The bactericidal effect of surface micro-discharge plasma under different ambient conditions" *New J. Phys.* **13** 023026 (2011) doi:10.1088/1367-2630/13/2/023026

[15] G. E. Morfill, T. Shimizu, B. Steffes, H.-U. Schmidt "Nosocomial infections—a new approach towards preventive medicine using plasmas" *New J. Phys.* **11** 115019 (2009) doi:10.1088/1367-2630/11/11/115019

[16] Y. Sakiyama, D. B. Graves, H.-W. Chang, T. Shimizu, G. E. Morfill "Plasma chemistry model of surface microdischarge in humid air and dynamics of reactive neutral species" *J. Phys. D: Appl. Phys.* **45** 425201 (2012) doi:10.1088/0022-3727/45/42/425201

[18] Z. C. Liu, D. X. Liu, C. Chen, D. Li, A. J. Yang, M. Z. Rong, H. L. Chen and M. G. Kong, "Physicochemical processes in the indirect interaction between surface air plasma and deionized water" *J. Phys. D: Appl. Phys.* **48** 495201 (2015) doi:10.1088/0022-3727/48/49/495201

[19] J. P. Boeuf and L. C. Pitchford "Electrohydrodynamic force and aerodynamic flow acceleration in surface dielectric barrier discharge" *Journal of Applied Physics* **97** 103307 (2005) doi: 10.1063/1.1901841

[20] J-J Wang , K-S Choi , L-H Feng a , T. N. Jukes, R. D. Whalley "Recent developments in DBD plasma flow control" Progress in Aerospace Sciences **62** 52 (2013) doi: 10.1016/j.paerosci.2013.05.003

[21] K. Takashima, Y. Zuzeek, W. R. Lempert and I. V. Adamovich "Characterization of a surface dielectric barrier discharge plasma sustained by repetitive nanosecond pulses" *Plasma Sources Sci. Technol.* **20** 055009 (2011) doi: 10.1088/0963-0252/20/5/055009

[22] G. J. M. Hagelaar, L. C. Pitchford "Solving the Boltzmann equation to obtain electron transport coefficients and rate coefficients for fluid models" *Plasma Sources Sci. Technol.* **14** 722 (2005) doi:10.1088/0963-0252/14/4/011, the version used of BOLSIG+ is dated 06-2013.

[23] MORGAN database, www.lxcat.net , retrieved on 20 December 2013

[a] *Y Sakiyama and D B Graves, Plasma Sources Sci. Technol., 22 (2013) 012003*

[24] F. Chen *Introduction to Plasma physics and controlled fusion*, 2nd edition Springer NY (2006)